# Robust half-metallicity and topological properties in square-net potassium manganese chalcogenides

Koushik Pradhan,[1] Prabuddha Sanyal,[2] and Tanusri Saha-Dasgupta [1,*]
[1]*Department of Condensed Matter and Materials Physics, S. N. Bose National Centre for Basic Sciences, JD Block, Sector III, Salt Lake, Kolkata, West Bengal 700106, India*
[2]*Department of Applied Physics, Maulana Abul Kalam Azad Univeristy of Technology, West Bengal 700064, India*

(Received 5 January 2023; revised 26 March 2023; accepted 28 March 2023; published 7 April 2023)

Combining *ab initio* and model Hamiltonian approaches, we investigate the electronic, magnetic, and topological properties of potassium manganese chalcogenides that host square nets of Mn and chalcogen atoms. Our analysis establishes these compounds to be robust half-metallic ferromagnets. The origin of ferromagnetism in these compounds is found to be based on a kinetic energy-driven double-exchange mechanism, first proposed for $Sr_2FeMoO_6$, a double-perovskite compound. The presence of finite spin-orbit coupling at chalcogen sites triggers nontrivial topology of the chalcogen-derived bands at the conducting channel, dominating the electronic structure close to the Fermi level. This puts the studied compounds in the class of topological half-metals with appreciable values of anomalous Hall conductivity, opening up the application possibility in topological quantum spintronics. Cleavability of these layered compounds makes the situation further promising.

DOI: 10.1103/PhysRevB.107.155115

## I. INTRODUCTION

Square-net compounds, consisting of two-dimensional layers of atoms forming square lattices, have been shown to exhibit many exciting properties. The best-known examples are cuprates with Cu atoms arranged in a square lattice, a motif that carries the genesis of high-temperature superconductivity [1]. The recently discussed Fe-based superconductors [2] as well as nickelates [3] also feature a square net of Fe and Ni atoms, respectively. Many intermetallic square-net compounds are found to exhibit diverse topological properties, like Dirac nodal-line semimetallicity as in $SrMnB_2$, $CaMnBi_2$, or $MXZ$ compounds like ZrSiS [4]. The family of synthesizable square-net materials are far from being complete, leaving this field a fertile ground for further exploration.

In this study, we focus on a family of ternary square-net chalcogenides, $KMnX_2$ ($X$ = Te, Se, and S) which consists of a square net of Mn atoms sandwiched between square nets of $X$ atoms, forming a trilayer. The trilayers are stacked along the vertical direction with K atoms intercalated between the trilayers. To compare the behavior of the chalcogen to its oxide counterpart, we also considered $X = \mathrm{O}$. Some of the compounds in this family have been synthesized [5,6]. However, to the best of our knowledge, no detailed work has been performed to explore the properties of these compounds. Keeping in mind the previous examples of connection of square-net geometry with exciting physical properties, it is worth investigating. The previous computational work indicated possible half-metallic behavior in some of these compounds [7], making the situation even more curious.

Half-metallicity, arising from the coexistence of the metallic behavior for one spin component and the insulating nature for the other, forms the basis of spintronics devices that relies on the generation of 100% spin-polarized current. Examples of half-metals include thiospinel systems [8], Heusler and full Heusler materials [9,10], double perovskites [11,12], and some oxides [13–15]. With the advent of topological electronic materials, attention has been drawn to topological quantum spintronics, which has the advantage of low-power consumption [16]. Magnetic topological insulators [17], exhibiting quantum anomalous Hall states with the internal magnetization breaking the time-reversal symmetry, have been discussed for topological quantum spintronics. Chern half-metals, which manifest the quantum anomalous Hall effect in one spin channel while being metallic in the other spin channel [18], have also been discussed. Considering the connection of square-net geometry to the nontrivial topology, along with possible half-metallicity in the potassium manganese compounds, these compounds hold the promise of serving as candidate materials for topological quantum spintronics.

Our first-principles calculations corroborated with model Hamiltonian studies establish that the chalcogen compounds of the studied series possess robust half-metallicity. The ferromagnetism is found to be driven by a two-sublattice double-exchange mechanism akin to that proposed for the double-perovskite $Sr_2FeMoO_6$ [19]. The finite spin-orbit coupling at $X$ atoms gives rise to topological behavior of the bands in the otherwise conducting spin channel, resulting in anomalous Hall conductivity. We further find these compounds are cleavable, with cleavage energy comparable with some of the existing two-dimensional compounds. This raises the hope for the possible use of these compounds in topological quantum spintronics.

*t.sahadasgupta@gmail.com

 

## II. METHOD AND COMPUTATIONAL DETAILS

The first-principles density functional theory (DFT) calculations were carried out in the plane-wave basis with projector augmented-wave potentials [20], as implemented in the Vienna *Ab initio* Simulation Package (VASP) [21]. The exchange-correlation functional was approximated within the generalized gradient approximation (GGA) of Perdew-Burke-Ernzerhof [22]. The electron-electron correlation at the transition-metal Mn site beyond the level of GGA was taken into account through a supplemented on-site Coulomb repulsion ($U$) and Hund exchange $J_H$ correction as implemented in Liechtenstein's multiorbital GGA + $U$ formalism [23]. Within the GGA + $U$ formulation of Liechtenstein, $U$ and $J_H$ are two parameters of the theory for which choices need to be made. Following the literature [24], we considered $U = 4$ eV and $J_H = 0.8$ eV on the Mn site. The obtained results have been checked by varying the $U$ value by 1–2 eV. A plane-wave energy cutoff of 600 eV and Brillouin zone sampling with $6 \times 6 \times 5$ Monkhorst-Pack grids were found to be sufficient for the convergence of energies and forces. For structural relaxations, ions were allowed to move until the atomic forces become less than 0.0001 eV/Å.

For the extraction of the few-band tight-binding Hamiltonian out of the full DFT calculation, to be used as the input to the model calculation, we carried out $N$th orbital muffin-tin orbital (NMTO) downfolding calculations [25]. The NMTO technique, which is not yet available in its self-consistent form, relies on the self-consistent potential parameters obtained out of linear muffin-tin orbital (LMTO) calculations[26] . The obtained results were cross-checked among the plane wave and LMTO calculations in terms of density of states (DOS) and band structures.

The topological properties were computed by using the WANNIER90 code [27]. For this, we first computed the maximally localized Wannier function (MLWF) to derive a tight-binding model from *ab initio* DFT calculations in the Mn-$d$–$X$-$p$ basis. Using the WANNIERTOOLS [28], the topological nature of the energy bands, near the Fermi level, were characterized by calculating the Chern number and the anomalous Hall conductivity.

The Berry curvature in the clean limit was calculated by using the Kubo formalism [29] given in the following equation,

$$\Omega_n^z(k) = -2\,\mathrm{Im} \sum_{m \neq n} \frac{\langle n|\hat{v}_x|m\rangle\langle m|\hat{v}_y|n\rangle}{(\epsilon_m - \epsilon_n)^2}, \tag{1}$$

where $\epsilon_m$ and $|m\rangle$ are the $m$th energy eigenvalue and eigenvector of the Hamiltonian, and $\hat{v}_x$ and $\hat{v}_y$ are the velocity operators along $x$ and $y$, respectively.

The Chern number was obtained by integration of the Berry curvature over the first Brillouin zone [29], as given below,

$$C_N = \frac{1}{2\pi} \sum_n \int_{\mathrm{BZ}} \Omega_n^z(k) d^2k, \tag{2}$$

where $\Omega_n^z(k)$ is the Berry curvature of the $n$th band at a specified $k$ point.

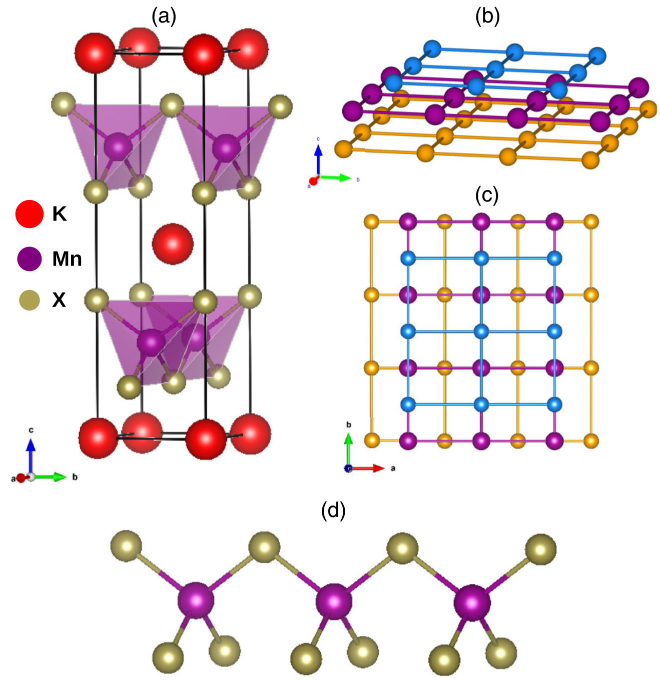


FIG. 1. (a) Conventional unit cell of $KMnX_2$ ($X$ = Te, Se, S, and O) in the $I\bar{4}m2$ (119) space group. (b) Side view of the stacking of Mn square planes, sandwiched between $X$ square planes. Blue and yellow colors denote upper and lower $X$ planes, respectively. (c) Top view of the stacking of Mn and $X$ planes. (d) Mn-$X$ network, with Mn atoms surrounded by $X$ atoms in a tetrahedral arrangements.

Anomalous Hall conductivity, arising from the Berry curvature, was computed employing the following equation [29],

$$\sigma_{xy} = -\frac{e^2}{\hbar} \sum_n \int_{\mathrm{BZ}} \frac{d^3k}{(2\pi)^3} \Omega_n^z(k) f_n, \tag{3}$$

where $f_n$ is the Fermi-Dirac distribution function and $\hbar$ is the reduced Planck's constant.

## III. RESULTS

### A. Crystal structure

$KMnX_2$ compounds crystallize in a tetragonal structure having the space group $I\bar{4}m2$ (119), with two formula units per unit cell [5,6]. As shown in Fig. 1, the primary structural motif is a trilayer, consisting of square nets of Mn atoms and $X$ atoms, with a middle layer of Mn atoms, sandwiched between an upper layer of $X$ atoms and a lower layer of $X$ atoms [cf. Figs. 1(b) and 1(c)]. This, in turn, puts Mn atoms in tetrahedral coordination with $X$ atoms, with corner sharing of $MnX_4$ units [cf. Fig. 1(d)]. The Mn-$X$ trilayers are stacked in a staggered fashion, as shown in Fig. 1(a), separated from each other by intercalated K atoms.

While $KMnTe_2$ and $KMnSe_2$ compounds have been synthesized [5,6], the S and O counterparts have yet to be synthesized. The crystal structures of $KMnS_2$ and $KMnO_2$ compounds are thus formed by starting with the crystal structure of $KMnSe_2$, replacing Se atoms by S and O and theoretically relaxing the structure completely including the volume and shape, keeping only the space group symmetry fixed. To be consistent, the calculations reported in the following are carried out on theoretically optimized structures for all four compounds. The theoretically optimized equilibrium structural parameters of $KMnTe_2$ and $KMnSe_2$ compounds are in good agreement with the experimental values [5,6]. The computed values of the lattice parameter $a$ and the equilibrium volume $V_0$ are found to deviate by less than 3.1% and 1.5%, respectively, from the experimentally measured values for $KMnTe_2$ and by less than 5.0% and 1.3%, respectively, from the measured values for $KMnSe_2$. Upon replacement of Te by S and O, $a$ and $V_0$ are found to progressively decrease by 12.8% to 27.4%, and about 30% and 58.3%, respectively. While the $M$-$X$-Mn angle does not show much variation across the $X =$ Te, Se, S, and O series with a value between 105° and 108°, the average Mn-$X$ bond lengths show a monotonic decrease, consistent with volume reduction, from 2.74 Å to 2.54 Å, to 2.4 Å, to 1.96 Å for Te, to Se, to S, to O. The variation of the structural parameters across the series are presented in the Supplemental Material (SM) [30].

### B. Stability

As mentioned, while $KMnTe_2$ and $KMnSe_2$ compounds have been synthesized, the S and O counterparts have yet to be synthesized. This makes validation of stability of the studied compounds crucially important. Both the thermodynamic stability and the dynamic stability need to be ascertained. A possible way to check the thermodynamic stability is through construction of a convex hull. An alternative way could be the finite-temperature molecular dynamics (MD) simulation. To check the thermal stability, we ran the MD simulation for all four compounds at 300 K. The resultant free energy over a time span of 20 ps (cf. SM [30]) is found to fluctuate around a constant value, signaling the thermodynamic stability of the $KMnX_2$ compounds. All four compounds are also found to be lattice dynamically stable, through the calculated phonon spectrum (see SM [30] and Ref. [31]). No imaginary phonon frequencies are observed, confirming the dynamical stability of $KMnX_2$ in the tetragonal phase.

We also calculated the formation energy of the compounds, defined as

$$E_{\mathrm{form}} = E(\mathrm{KMn}X_2) - (\mu_K + \mu_{\mathrm{Mn}} + 2 \times \mu_X),$$

where $E(\mathrm{KMn}X_2)$ is the total energy of the $\mathrm{KMn}X_2$ compound, and $\mu_K$, $\mu_{\mathrm{Mn}}$, and $\mu_X$ are the chemical potentials of the K atom, the Mn atom, and the $X$ atom, respectively, which are taken as total energies per atom of BCC K crystal, BCC Mn crystal, and orthorhombic and trigonal crystals of S and Se/Te, respectively. For $X =$ O, it is calculated from the total energy of the $O_2$ molecule. The calculated formation energies are found to be $-1.14$ eV for $KMnTe_2$, $-1.98$ eV for $KMnSe_2$, $-2.52$ eV for $KMnS_2$, and $-3.96$ eV for $KMnO_2$.

### C. Electronic structure

The spin-polarized DOS, calculated within the GGA + $U$ and projected onto Mn-$d$ and $X$-$p$ states, are shown in Fig. 2. Figure 2(a) shows the DOS plot for $KMnTe_2$ in the wide energy range of $-5.0$ to 5.0 eV around the Fermi energy ($E_f$). The density of state plot reveals some striking features. First,

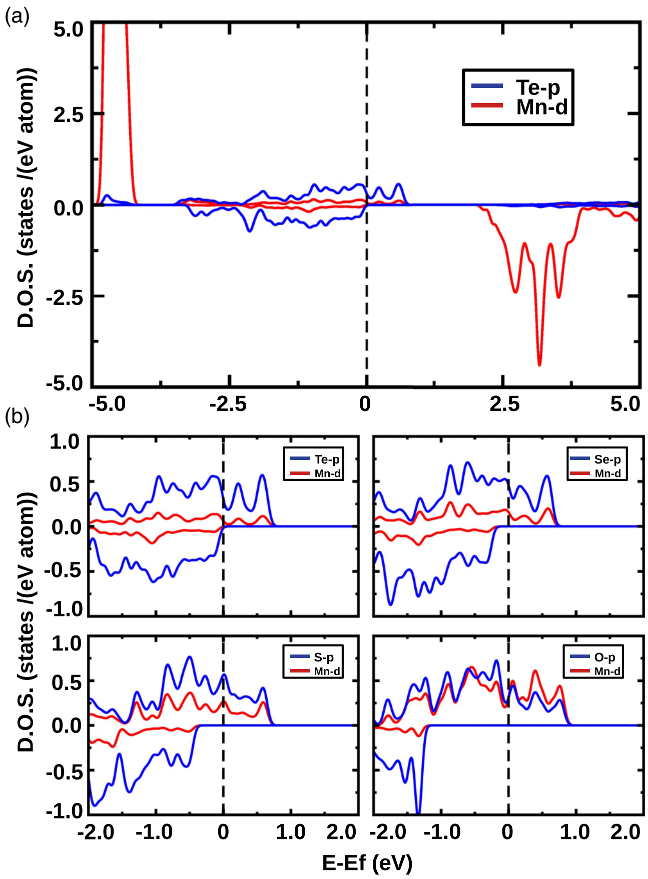


FIG. 2. (a) Spin-polarized GGA + $U$ density of states of $KMnTe_2$, projected onto Mn-$d$ and Te-$p$ states. Energies were measured with respect to the GGA + $U$ Fermi energy. (b) Zoomed in plots of the density of states for $\mathrm{KMn}X_2$ ($X =$ Te, Se, S, and O), projected into Mn-$d$ (red) and X-$p$ (blue) states.

as opposed to the expected nominal valence of $Mn^{3+}$, with $d^4$ occupancy, we find that Mn-$d$ states are mostly occupied in the majority spin channel and empty in the minority spin channel, suggestive of a $Mn^{2+}$ nominal valence with $d^5$ occupancy. Second, in contrast to the essentially nonmagnetic nature of $Te^{2-}$ anions, the Te-$p$ states are found to be strongly spin split, dominating the electronic structure close to $E_f$, which is half-metallic in the sense it is insulating with a gap of about 1–2 eV in the minority spin channel and conducting in the other spin channel. The DOS zoomed to $E_f$ over an energy range of $-2$ to 2 eV for $KMnTe_2$, $KMnSe_2$, $KMnS_2$, and $KMnO_2$ are shown in Fig. 1(b). We find that in all cases the $X$-$p$ states are strongly spin split and dominate the half-metallic electronic structure close to $E_f$ [32]. However, the dominance of low-energy $X$-$p$ states over Mn-$d$ states progressively decreases as one moves from Te to Se to S to O. In order to quantify the above, we computed the ratio of the projected DOS onto $X$-$p$ and Mn-$d$ states at $E_f$ [cf. Fig. 3(a)]. This measure, $\rho_X/\rho_{\mathrm{Mn}}$, is found to be as large as 5 for $KMnTe_2$, about 3 for $KMnSe_2$, and about 2 for $KMnS_2$. For $KMnO_2$, the contribution of Mn-$d$ states at $E_f$ becomes almost equal to that of O-$p$, with $\rho_O/\rho_{\mathrm{Mn}}$ reaching a value close to 1. This trend is further corroborated by the calculated magnetic

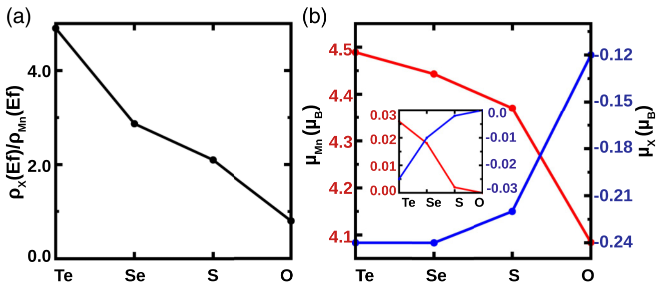


FIG. 3. (a) Ratio of density of states at Fermi energy, projected to $X$-$p$ and Mn-$d$ [$\rho_X(E)/\rho_{\mathrm{Mn}}(E)$], plotted for the four compounds. (b) Magnetic moments ($\mu_B$) at Mn (red, left $y$ axis) and $X$ (blue, right $y$ axis) sites. The inset shows the orbital moments ($\mu_B$) at Mn and $X$ sites. The convention is the same as that in the main panel.

moments at Mn and $X$ sites [cf. Fig. 3(b)]. The magnetic moments at Mn sites are found to be larger than 4 $\mu_B$, the moment expected considering $Mn^{3+}$ nominal valence. At the same time, an unusually large moment is found at $X$ sites, aligned in the direction opposite to that of the Mn moment. A moment of 4.5–4.4 $\mu_B$ is found at the Mn site with an oppositely aligned moment of about 0.2 $\mu_B$ at $X$ sites, for the chalcogen series $X$ = Te, Se, and S. In contrast, for the oxide, the magnetic moment at the Mn site reduces to 4.1 $\mu_B$ with an oppositely aligned moment at the O site reduced to about 0.1 $\mu_B$. The resulting total moment in each case turned out to be 4.0 $\mu_B$. The above observations point towards two things in the chalcogen $KMnX_2$: (i) The nominal valence of Mn in these compounds is 2+, rather than 3+, as expected considering a nominal valence of 2− at the $X$ sites, and (ii) a large induced moment develops at otherwise nonmagnetic $X$ sites, which is oppositely aligned to Mn moments. These two observations are in striking similarity with the hybridization-driven two-sublattice double-exchange mechanism of magnetism, first proposed for the double-perovskite $Sr_2FeMoO_6$ [19], which shows an induced moment at otherwise nonmagnetic Mo sites driven by the hybridization between itinerant Mo-$d$ electrons and the large Fe core $S = 5/2$ core spins. We investigate this issue in detail in the next subsection.

Since the compounds among the studied series, especially the chalcogen compounds, contain elements like Te, Se, and S, we further investigated the effect of spin-orbit coupling (SOC) on the electronic structure and magnetic moments. The computed electronic structure is found to exhibit a sustained half-metallic nature even in the presence of SOC, confirming its robustness. The inset in Fig. 3(b) shows the orbital moments at Mn and $X$ sites, both of which turn to be oriented in the same direction as the corresponding orbital moment, due to their more than half-filled nature. Non-negligible orbital moments are found for chalcogen compounds. It is to be noted that the calculated half-metallic behavior can be influenced by the choice of exchange-correlation functional as well as by the strain. The computed half-metallic character of all the compounds, however, is found to survive for the choice of different exchange-correlation functionals, as explicitly checked for the GGA and the GGA + $U$ with choice $U$ value of 1–6 eV, as well as for the Heyd-Scuseria-Ernzerhof functional [33]. The half-metallic behavior is further found to survive upon application of both tensile and compressive strains of 2%–4%.

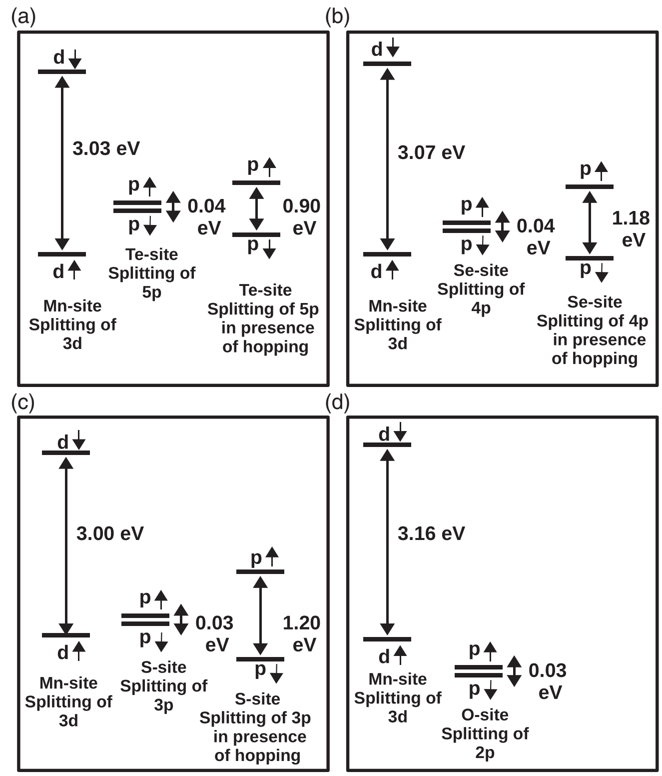


FIG. 4. Panels (a)–(d) show the spin-polarized splitting, with and without $d - p$ hybridization, of $KMnTe_2$, $KMnSe_2$, $KMnS_2$, and $KMnO_2$ compounds, respectively.

### D. Mechanism of magnetism

In order to get an insight into the mechanism of magnetism in $KMnX_2$ compounds, we next carried out calculations employing the muffin-tin orbital based technique of NMTO downfolding. NMTO-downfolding calculations enable defining energy-selected, effective Wannier functions by integrating out degrees of freedom that are not of interest (*downfolding*). To unravel the mechanism, we first downfolded all the degrees of freedom, except Mn-$d$ and $X$-$p$. The on-site block of the real-space description of this Hamiltonian provides information on on-site energies of Mn-$d$ and $X$-$p$, their relative alignment, and their intrinsic spin-splitting. In the second step, we applied massive downfolding, keeping only $X$-$p$ degrees of freedom active and downfolding all the rest including Mn-$d$ degrees of freedom. The on-site block of the real-space description of this massive downfolding gives information on $X$-$p$ energy levels, and its spin splitting, induced by the hybridization between Mn-$d$ and $X$-$p$. Figure 4 summarizes the positioning of the energy levels of the four compounds in the Mn-$d$–$X$-$p$ and massively downfolded, renormalized $X$-$p$ basis, as given by NMTO-downfolding calculations. Mn-$d$ states are both crystal field split and spin-split. The tetragonal environment of $X$ atoms, surrounding Mn, splits the Mn-$d$ states into $t_2$ ($d_{xy}$, $d_{xz}$, $d_{yz}$) and $e$ ($d_{3z2}$, $d_{x^2-y^2}$), which due to elongation of the $MnX_4$ tetrahedra split further into $d_{xy}$, ($d_{xz}$, $d_{yz}$), $d_{3z2}$, and $d_{x^2-y^2}$. However, the crystal field splittings turn out to be much weaker compared to the large spin-splitting at the Mn site due to the large core spin of $S = 5/2$. In Fig. 4, for simplicity, we thus show the average Mn-$d$ position, ignoring the crystal field splitting. The same is true for $X$-$p$ levels. Remarkably, we find that in the Mn-$d$–$X$-$p$ basis, $X$-$p$ states are essentially nonmagnetic with small spin-splitting of 0.03–0.04 eV, which lie within the large energy interval of ∼3 eV of the strongly spin-split states of Mn-$d$, except for the oxygen compound. Interestingly, the $X$-$p$ levels move downwards compared to Mn-$d$ in moving from Te to Se to S, and finally for $X = \mathrm{O}$, the $X$-$p$ levels are pushed out of the Mn-$d$ spin-split energy window. In the massively downfolded $X$-$p$ basis, which takes into account the hybridization between Mn-$d$ and $X$-$p$, an induced spin-splitting of ∼1 eV develops at $X$ sites oppositely aligned to the spin-splitting of Mn-$d$. Upon switching on the Mn-$d$–$X$-$p$ hybridization, the states of the same spin interact, and due to the positioning of the $X$-$p$ states within the window of the spin-split Mn-$d$, this pushes the up-spin $X$-$p$ energy levels further up and the down-spin $X$-$p$ energy levels further down. These opposite movements of $X$-$p$ up-spin and $X$-$p$ down-spin energy levels increase the energy separation between these two levels, thereby resulting in a renormalized, negative spin-splitting at an otherwise nonmagnetic $X$ site. While this scenario is found to be true for all three chalcogenides, the scenario for the oxygen compound is found to be markedly different. For the oxygen compound, since the $p$ levels of oxygen lie outside the exchange gap of the Mn spin-split $d$ levels, the mechanism of double exchange is not valid, rather the magnetism is governed by the conventional Heisenberg superexchange.

Based on the above, we constructed a two-site double-exchange model for the chalcogen compounds, consisting of (i) a large core spin of $S = 5/2$ at the Mn site, (ii) strong coupling on the Mn site between the core spin and the itinerant electron, strongly preferring one spin polarization of the itinerant electron, and (iii) delocalization of the itinerant electron on the Mn-$X$ network.

The model Hamiltonian, considering two $X$ atoms and one Mn atom in the basis, is thus given as follows:

$$H = \epsilon_{\mathrm{Mn}} \sum_{i\sigma} m_{i\sigma}^{\dagger} m_{i\sigma} + \epsilon_X \sum_{i\alpha\sigma} x_{i\sigma}^{\alpha\dagger} x_{i\sigma}^{\alpha} + t \sum_{i\delta\alpha\sigma} m_{i\sigma}^{\dagger} x_{i+\delta_\alpha,\sigma}^{\alpha} + J \sum_{i\mu\nu} \vec{S}_i \cdot m_{i\mu}^{\dagger} \vec{\sigma}_{\mu\nu} m_{i\nu}, \tag{4}$$

where $\alpha = 1$ and 2 represents two $X$ atoms, $\delta_\alpha = \hat{i}a$ for $\alpha = 1$ and $\delta_\alpha = \hat{j}a$ for $\alpha = 2$. $m$ represents the Mn-$d$ degrees of freedom, while $x$ represents the $p$ orbital degrees of freedom of the $X$ atom. For simplicity, we neglected the multiorbital nature of Mn-$d$ and $X$-$p$. $t$ is the average Mn-$X$ hopping in this simplified, single-orbital model, while $J$ is the exchange (Kondo coupling) on the Mn site. Considering two $X$ atoms and a Mn atom in the basis, this gives rise to $3 \times 2 = 6$ degrees of freedom per formula unit, which includes spin. The values of the average on-site energies for Mn ($\epsilon_{\mathrm{Mn}}$) and $X$ ($\epsilon_X$) and the hopping $t$ are obtained from the low-energy, tight-binding Hamiltonian obtained from NMTO downfolding. The exchange $J$ is obtained from the average exchange gap of Mn-$d$ levels from the energy level diagram mentioned above.

The constructed model Hamiltonian was solved by the exact diagonalization (ED) technique on a two-dimensional

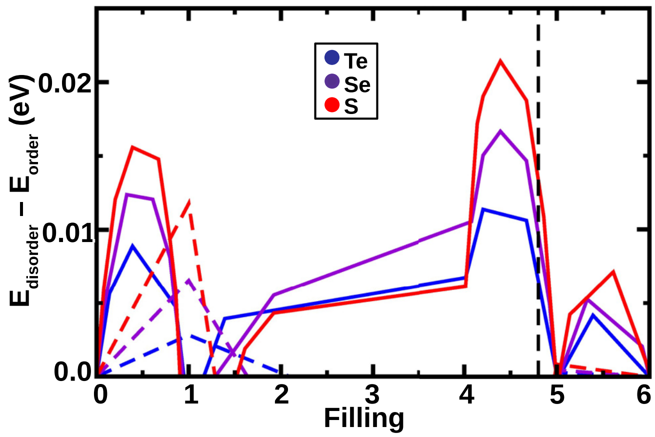


FIG. 5. $E_{\mathrm{disord}}$-$E_{\mathrm{ord}}$ vs electron filling for FM and G-AFM phases obtained from ED for all the compounds. Blue, violet, and red colors appear for $KMnTe_2$, $KMnSe_2$, and $KMnS_2$ compounds, respectively. The solid line corresponds to the FM ordered phase and the dashed line corresponds to the G-AFM ordered phase. The filling of interest, $n \approx 4.8$, is marked by a black vertical dashed line.

$16 \times 16$ lattice. For modeling of magnetic properties, we consider a two-dimensional (2D) geometry, as the interlayer Mn-Mn interaction via the spacer K atoms turned out to be small. This is further justified by the calculated cleavage energies, which are presented later.

We considered two different spin arrangements of the Mn core spins, ferromagnetic (FM) and G-type antiferromagnet (AFM), and measured their energies with respect to a spin disordered phase. The energetics of the four compounds are shown in Fig. 5, plotted as a function of the filling ($n$). We varied the filling range from 0 to 6, with 6 being the maximum filling possible in this 6 degrees of freedom model. The $\Delta E$-$n$ phase diagram shows sequences of ferromagnetic phases, with intervening AFM phases. The filling corresponding to actual compounds is 4.8, at which all three compounds exhibit stabilization of the ferromagnetic phase. Due to the proximity of the AFM phase, it may be interesting to drive the FM-AFM transition by doping, as achieved by La doping in $Sr_2FeMoO_6$ [34]. Notably, this antiferromagnetic state, driven by a hybridization-assisted mechanism, will be metallic. Mapping the FM energy difference from the spin disordered phase to the mean field $T_c$, one obtains the values 145, 116, and 58 K for the S, Se, and Te compounds, respectively.

### E. Topological properties

Having established the robust ferromagnetism in potassium manganese chalcogenides, we next explore the topological properties of the spin-split bands. $KMnX_2$ are centrosymmetric crystals and so are inversion symmetry invariant. However, the time-reversal symmetry is broken due to the presence of ferromagnetic order. This, together with nonzero SOC at $X$ sites, opens up the possibility of a nontrivial Chern number of the bands near $E_f$, which are primarily $X$-$p$ bands, with some amount of admixture of Mn-$d$. We focus only on the majority spin channel, as minority spin states are 1–2 eV far from $E_f$. Figures 6(a)–6(c) show the band dispersion computed in the absence of SOC, in the majority spin channel

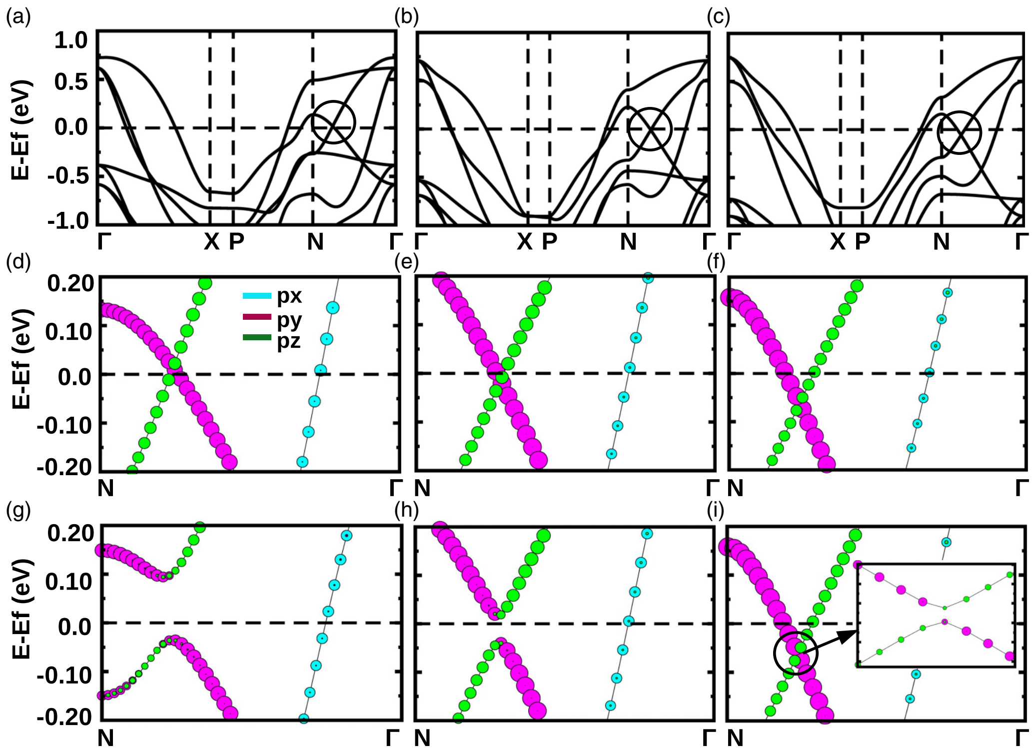


FIG. 6. Panels (a)–(c) show GGA band structures, along the high-symmetry points of BZ Γ = (0 0 0), X = (0 0 0.5), P = (0.25 0.25 0.25), N = (0.0 0.5 0.0), and Γ = (0 0 0), for Te, Se, and S compounds, respectively. Panels (d)–(f) show orbital-projected [projected on $p_x$, $p_y$, and $p_z$ orbitals of ligand atoms ($X$)] GGA band structures along N to Γ, near the Fermi level, for Te, Se, and S compounds, respectively. Panels (g)–(i) show orbital-projected (projected on $p_x$, $p_y$, and $p_z$ orbitals of $X$) GGA + SOC band structures along N to Γ, near the Fermi level, for Te, Se, and S compounds, respectively. Cyan, magenta, and green colors stand for $p_x$, $p_y$, and $p_z$ orbitals, of ligand atoms, respectively.

along the high-symmetry paths of the primitive BZ of the tetragonal lattice, with Γ = (0 0 0), X = (0 0 0.5), P = (0.25 0.25 0.25), and N = (0.0 0.5 0.0). Low-energy Dirac-like crossing (encircled) in the figure is observed between N and Γ for all three compounds, which are energetically found to lie within 200–100 meV around $E_f$. Figures 6(d)–6(f) show the zoomed-in plot of band dispersion from N to Γ, with orbital characters projected to $X$-$p_x$, $X$-$p_y$, and $X$-$p_z$. Figures 6(g)–6(i) show the same upon switching on SOC. As is seen from the orbital character projected band structures, the crossing at $\mathbf{k}_c = (0, 0.35, 0)$, between the high-symmetry points N and Γ arises due to the intersection of bands of two different orbital characters, $p_z$ and $p_y$. Upon inclusion of SOC, a band anticrossing happens, resulting in a change of the band orbital character of the two bands involved in forming the crossing, as the **k** vector changes from a smaller value to a value larger than that of $\mathbf{k}_c$ [35]. As discussed in the context of materials like LaBi [36,37], such a SOC-driven anticrossing can open up a topological gap. The band derived out of the $p_x$ character, on the other hand, is highly dispersive, does not mix with $p_z$ or $p_y$, and as a single band cuts the Fermi level. In order to further check the topological nontriviality of the pair of bands forming the anticrossing, we calculated the topological invariant. To ascertain the nontriviality of anticrossing points specifically, we first calculated the contribution of the Berry curvature for the pair of bands forming the anticrossing, by employing Eq. (1) where $n$ and $m$ were chosen to be 15 and 16, the two bands forming the anticrossing. The Chern number was computed subsequently by integrating the abovementioned Berry curvature [cf. Eq. (2)] over a 2D plane in reciprocal space. Considering the layered structure of the compounds, we choose the 2D plane to a K1-K2 plane in the reciprocal space with K3 = 0 (cf. inset in Fig. 7). The chosen K1-K2 plane includes the high-symmetry points N and Γ, as the anticrossing point lies in between N and Γ along K2. Integration of the Berry curvature arising from the bands forming the anticrossing over this 2D plane resulted in a Chern number with an integer value of 1 for all three compounds. Thus, the pair of bands forming the anticrossing are of nontrivial topology. It is to be noted that the Chern number $C$ is well defined in the insulator state, being an integer. As mentioned above, the Chern number in the present context is calculated for a specific pair of bands forming the anticrossing, which are well separated from each other at all momenta. These two bands in the presence of SOC, though they are separated from each other at every momentum, cross the Fermi level along with other trivial bands. As can be easily understood, it is complicated to calculate the Chern numbers of the individual bands since they cross. A more robust quantity is the anomalous Hall response of the resultant metal with nontrivial topology, as discussed below. The electrons see an extra source of Berry flux due to this nontrivial band topology of the Chern bands, which is responsible for the anomalous Hall conductivity. The corresponding Berry curvature, together with band dispersion along N-Γ, is shown in the top two rows of Fig. 7. The Berry curvature, shown in Fig. 7, is computed considering the pair of bands forming the anticrossing. As these bands also

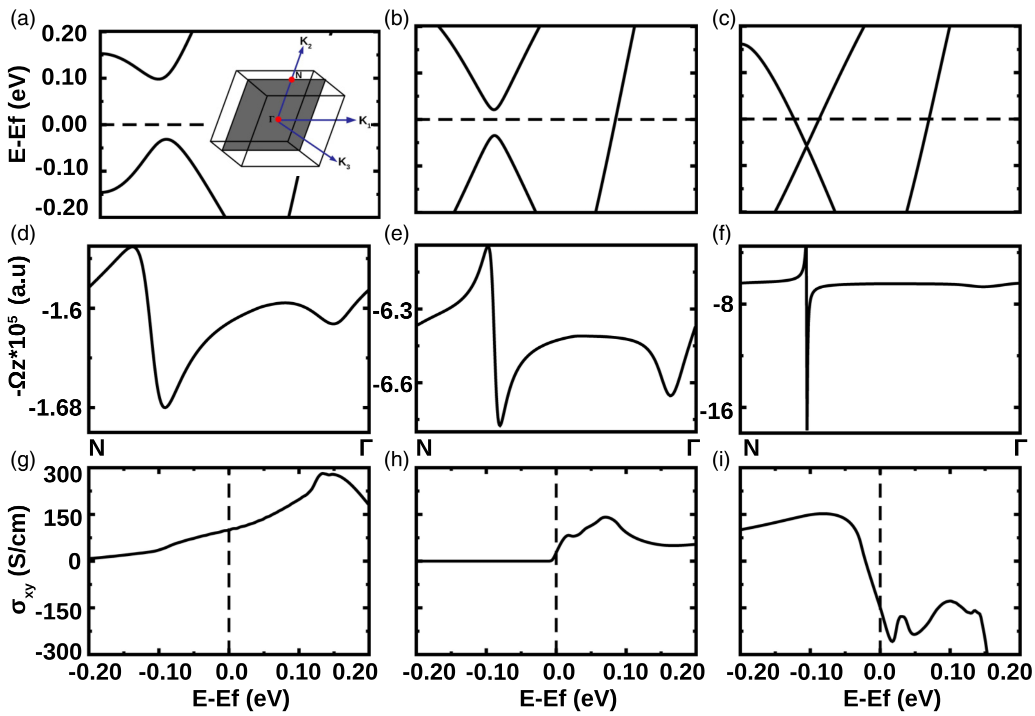


FIG. 7. (a)–(c) GGA + SOC band structures, along N to Γ, for Te, Se, and S compounds, respectively. The inset in panel (a) shows the 3D BZ along with the 2D plane, over which the BZ intergration is carried to compute the Berry curvature of the anticrossing pair of bands. (d)–(f) $z$th component of the Berry curvature, along N to Γ, for Te, Se, and S compounds, respectively, contributed by anticrossing bands. (g)–(i) The anomalous Hall conductivity, in a narrow energy window around $E_f$, for Te, Se, and S compounds, respectively.

cross with other bands, the calculation was also carried out considering the entire subset of bands crossed by these bands which are trivial in nature. The contribution of other bands in the Berry curvature is found to be small. In particular, the effect of other bands is found to be negligible at the anticrossing point, where the Berry curvature peaks. The calculated intrinsic anomalous Hall conductivity (AHC), $\sigma_{xy}$, obtained by integrating the Berry curvature over k-space and considering the bands up to energy $E$, is shown in Figs. 7(g)–7(i) for the three compounds, plotted as a function of $E$, measured from $E_f$. The values at $E_f$ turned out to be 100, 28, and 153 $\Omega^{-1}$ cm$^{-1}$ for $KMnTe_2$, $KMnSe_2$, and $KMnS_2$ respectively, the values being comparable to currently studied topological magnetic materials [38], especially for Te and S compounds. The maximum contribution to the Berry curvature is found to arise from the nontrivial Chern bands, as rigorously checked by computing the Berry curvature for other pair of bands as well. Focusing on the S compound, for which the AHC turned out to be the largest, we do see that the AHC [cf. Fig. 7(i)] has small, modest values at energies below the Fermi level and attains a large value only close to the Fermi level arising from the nontrivial band topology. An important point to note here is that the topological nontriviality contributing in AHC arises solely out of the majority spin channel, because due to the half-metallic nature of the band structure even in the presence of SOC, the states near $E_f$ are contributed only by up-spin. This makes the compounds a new class of topological materials which are metal with nontrivial topology [39] in one spin channel and insulator in the other spin channel. This is in contrast to the proposed Chern half-metals which host the Chern insulating state in one spin channel and are metallic in the other spin channel, as discussed for Co- or Rh-deposited graphene [18].

### F. Cleavage energy

Given the exciting magnetic and topological properties of $KMnX_2$ chalcogenides, and the prospect of topological quantum spintronics, it will be further beneficial if the studied compounds can be cleaved to produce quasi-2D layers. Possible means to derive the 2D counterparts from the 3D layered structures are through mechanical or chemical routes. An energy barrier needs to be overcome, in this respect, known as cleavage energy. Cleavage energy [40] is the energy required to create two (top and bottom) surfaces by cleaving the bulk compounds along the desired plane, $E_{\rm cl} = 2\frac{(E_{\rm slab}-E_{\rm bulk})}{2A}$, where $E_{\rm slab}$ is the total energy of the cleaved system with two bare surfaces, $E_{\rm bulk}$ is the total energy of the same in the bulk system, and $A$ is the surface area. We computed the cleavage energies for $KMnX_2$ compounds by considering the cleavage plane through the K site and computing the area-normalized energy differences between the layer-separated and the bulk compounds upon increasing the interlayer separation until the individual layers were sufficiently far that the dispersive interactions were negligible. Figure 8(a) shows the estimated cleavage energies. It is encouraging to note that, except for $KMnO_2$ ($E_{\rm cl} = 3.05$ J/m$^2$), the computed $E_{\rm cl}$ values for $KMnX_2$ are reasonably small (0.92, 1.31, and 1.61 J/m$^2$ for $KMnTe_2$, $KMnSe_2$, and $KMnS_2$, respectively). These values are found to be comparable with some of the layered compounds reported earlier [41–49], as shown in Fig. 8(b). While these compounds are not van der Waals compounds, the

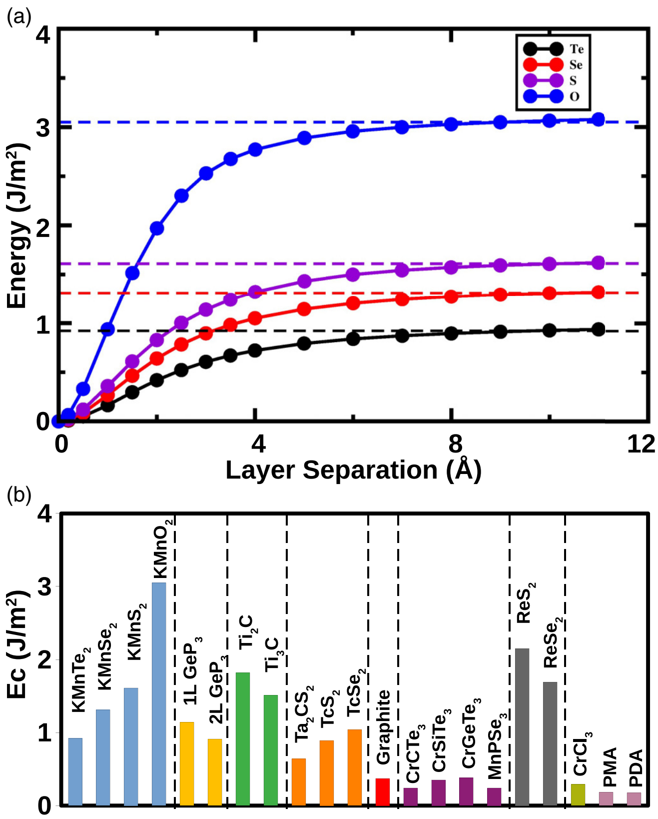


FIG. 8. (a) Cleavage energies of $KMnX_2$ ($X$ = Te, Se, S, and O). (b) Comparison of the cleavage energies with other existing 2D materials.

2D counterparts may be obtained through chemical etching, as followed for creating 2D MXenes from the 3D MAX phases [49,50].

The magnetic ground states of the cleaved layers continued to be ferromagnetic, enhancing the prospect of these compounds in topological quantum spintronics.

## IV. SUMMARY

Motivated by the reported exciting physical properties offered by square-net geometry compounds, in this study we explore the electronic, magnetic, and topological properties of Mn-based square-net compounds $KMnX_2$. While a few of the members of this family have been synthesized, the corresponding study of physical properties has remained limited. Our first-principles study combining the *ab initio* and derived model Hamiltonian approaches reveals rich properties of this yet-to-be explored family. In particular, our study establishes robust half-metallicity in these compounds, driven by a two-sublattice double-exchange mechanism that arises due to the positioning of essentially nonmagnetic X-$p$ levels within the strongly spin-split levels of Mn $S = 5/2$. This results in an induced negative spin polarization at otherwise nonmagnetic $X$ sites, forcing all the Mn spins to be aligned parallel. This Mn-$d$–$X$-$p$ hybridization-driven mechanism is akin to that of $Sr_2FeMoO_6$, although the underlying geometries are very different. The half-metallic bands close to $E_f$ and dominated by $X$-$p$ give rise to a Dirac-like anticrossing formed by degenerate $p_y$ and $p_z$ orbitals, carrying nontrivial Chern numbers of 1. The calculated anomalous Hall conductivity is found to be comparable with the recently studied topological magnetic materials. Thus, these compounds are topological half-metals, with a metallic character of nontrivial topology in one spin channel and an insulating character in the other spin channel. This is distinct from recently proposed Chern half-metals, which are a Chern insulator in one spin channel and metallic in the other. Calculated cleavage energy further showed that the exfoliation of these compounds in 2D layers is possible, enabling the prospect of quantum topological spintronics applications. We hope our study will motivate future exploration of this promising class of compounds.

## ACKNOWLEDGMENTS

T.S.-D. acknowledges the J. C. Bose National Fellowship (Grant No. JCB/2020/000004) for funding.

[1] R. J. Cava, Oxide superconductors, Am. Ceram. Soc. **83**, 5 (2000); H. Shaked, *Crystal Structures of the High-Tc Superconducting Copper-Oxides* (Elsevier, Amsterdam, 1994).

[2] J. Paglione and R. Greene, High-temperature superconductivity in iron-based materials, Nat. Phys. **6**, 645 (2010).

[3] R. M. Wilson, Superconductivity is found in a nickel oxide, Phys. Today **72**(11), 19 (2019).

[4] S. Klemenz, S. Lei, and L. M. Schoop, Topological semimetals in square-net materials, Annu. Rev. Mater. Res. **49**, 185 (2019).

[5] J. Kim and T. Hughbanks, Synthesis and structures of new layered ternary manganese selenides: $AMnSe_2$ ($A$= Li, Na, K, Rb, Cs) and $Na_2Mn_2Se_3$, J. Solid State Chem. **146**, 217 (1999).

[6] J. Kim, C. Wang, and T. Hughbanks, Synthesis and structures of new layered ternary manganese tellurides: $AMnTe_2$ (A = K, Rb, Cs), $Na_3Mn_4Te_6$, and $NaMn_{1.56}Te_2$, Inorg. Chem. **38**, 235 (1999).

[7] A. Benmakhlouf, A. Bentabet, A. Bouhemadou, and A. Benghia, Prediction of half-metallic properties for the $AMnSe_2$ ($A$ = Rb, Cs) compounds from first-principle calculations, J. Magn. Magn. Mater. **399**, 179 (2016).

[8] M. S. Park, S. K. Kwon, and B. I. Min, Half-metallic antiferromagnets in thiospinels, Phys. Rev. B **64**, 100403(R) (2001).

[9] I. Galanakis, P. H. Dederichs, and N. Papanikolaou, Origin and properties of the gap in the half-ferromagnetic Heusler alloys, Phys. Rev. B **66**, 134428 (2002).

[10] I. Galanakis, P. H. Dederichs, and N. Papanikolaou, Slater-Pauling behavior and origin of the half-metallicity of the full-Heusler alloys, Phys. Rev. B **66**, 174429 (2002).

[11] D. D. Sarma, P. Mahadevan, T. Saha-Dasgupta, S. Ray, and A. Kumar, Electronic Structure of $Sr_2FeMoO_6$, Phys. Rev. Lett. **85**, 2549 (2000).

[12] K. I. Kobayashi, T. Kimura, H. Sawada, K. Terakura, and Y. Tokura, Room-temperature magnetoresistance in an oxide material with an ordered double-perovskite structure, Nature (London) **395**, 677 (1998).

[13] K. Schwarz, $CrO_2$ predicted as a half-metallic ferromagnet, J. Phys. F: Met. Phys. **16**, L211 (1986).

[14] D. Ködderitzsch, W. Hergert, Z. Szotek, and W. M. Temmerman, Vacancy-induced half-metallicity in MnO and NiO, Phys. Rev. B **68**, 125114 (2003).

[15] H. Wu, Y. Qian, W. Tan, C. Xiao, K. Deng, and R. Lu, The theoretical search for half-metallic material: The non-stoichiometric peroskite oxide $Sr_2FeCoO_{6-\delta}$, Appl. Phys. Lett. **99**, 123116 (2011).

[16] Q. L. He, T. L. Hughes, N. P. Armitage, Y. Tokura, and K. L. Wang, Topological spintronics and magnetoelectronics, Nat. Mater. **21**, 15 (2022).

[17] C. Z. Chang, J. Zhang, X. Feng, J. Shen, Z. Zhang, M. Guo, K. Li, Y. Ou, P. Wei, L.-L. Wang *et al.*, Experimental observation of the quantum anomalous Hall effect in a magnetic topological insulator, Science **340**, 167 (2013).

[18] J. Hu, Z. Zhu, and R. Wu, Chern half metals: A new class of topological materials to realize the quantum anomalous Hall effect, Nano Lett. **15**, 2074 (2015).

[19] D. D. Sarma, Sugata Ray, K. Tanaka, M. Kobayashi, A. Fujimori, P. Sanyal, H. R. Krishnamurthy, and C. Dasgupta, Intergranular Magnetoresistance in $Sr_2FeMoO_6$ from a Magnetic Tunnel Barrier Mechanism across Grain Boundaries, Phys. Rev. Lett. **98**, 157205 (2007).

[20] P. E. Blöchl, Projector augmented-wave method, Phys. Rev. B **50**, 17953 (1994).

[21] G. Kresse and J. Hafner, *Ab initio* molecular dynamics for liquid metals, Phys. Rev. B **47**, 558 (1993); G. Kresse and J. Furthmüller, Efficient iterative schemes for *ab initio* total-energy calculations using a plane-wave basis set, *ibid.* **54**, 11169 (1996).

[22] J. P. Perdew, J. A. Chevary, S. H. Vosko, K. A. Jackson, M. R. Pederson, D. J. Singh, and C. Fiolhais, Erratum: Atoms, molecules, solids, and surfaces: Applications of the generalized gradient approximation for exchange and correlation, Phys. Rev. B **48**, 4978(E) (1993).

[23] A. I. Liechtenstein, V. I. Anisimov, and J. Zaanen, Density-functional theory and strong interactions: Orbital ordering in Mott-Hubbard insulators, Phys. Rev. B **52**, R5467 (1995).

[24] L. Wang, T. Maxisch, and G. Ceder, Oxidation energies of transition metal oxides within the GGA + U framework, Phys. Rev. B **73**, 195107 (2006).

[25] O. K. Andersen and T. Saha-Dasgupta, Muffin-tin orbitals of arbitrary order, Phys. Rev. B **62**, R16219 (2000).

[26] O. K. Andersen and O. Jepsen, Explicit, First-Principles Tight-Binding Theory, Phys. Rev. Lett. **53**, 2571 (1984).

[27] A. A. Mostofi, J. R. Yates, G. Pizzi, Y. S. Lee, I. Souza, D. Vanderbilt, and N. Marzari, An updated version of wannier90: A tool for obtaining maximally-localised Wannier functions, Comput. Phys. Commun. **185**, 2309 (2014).

[28] Q. Wu, S. Zhang, H. F. Song, M. Troyer, and A. A. Soluyanov, WannierTools: An open-source software package for novel topological materials, Comput. Phys. Commun. **224**, 405 (2018).

[29] M. Gradhand, D. V. Fedorov, F. Pientka, P. Zahn, I. Mertig, and B. L. Györffy, First-principle calculations of the Berry curvature of Bloch states for charge and spin transport of electrons, J. Phys.: Condens. Matter **24**, 213202 (2012).

[30] See Supplemental Material at http://link.aps.org/supplemental/10.1103/PhysRevB.107.155115 for detailed information on structure, phonons, and MD simulation.

[31] A. Togo and I. Tanaka, First principles phonon calculations in materials science, Scr. Mater. **108**, 1 (2015).

[32] It is curious to note that the DOS of $KMnS_2$ shows a peakat $E_f$, while that of $KMnTe_2$ or $KMnSe_2$ shows a dip. Driven by the detailed nature of Mn-$X$ covalency, the DOS in general shows successive peaks and dips. However, the $E_f$ shows a shift between $KMnTe_2$ or $KMnSe_2$ and $KMnS_2$, resulting in a dip at $E_f$ for $KMnTe_2$ and $KMnSe_2$, while showing a peak at $E_f$ for $KMnS_2$. This shift is found to arise from the change of magnetic moment at the $X$ site between $KMnTe_2$ or $KMnSe_2$ and $KMnS_2$ [see Fig. 3(b)].

[33] J. Heyd, G. E. Scuseria, and M. Ernzerhof, Hybrid functionals based on a screened Coulomb potential, J. Chem. Phys. **118**, 8207 (2003).

[34] S. Jana, C. Meneghini, P. Sanyal, S. Sarkar, T. Saha-Dasgupta, O. Karis, and S. Ray, Signature of an antiferromagnetic metallic ground state in heavily electron-doped $Sr_2FeMoO_6$, Phys. Rev. B **86**, 054433 (2012).

[35] C. M. Acosta, E. Ogoshi, A. Fazzio, G. M. Dalpian, and A. Zunger, The Rashba scale: Emergence of band anti-crossing as a design principle for materials with large Rashba coefficient, Matter **3**, 145 (2020).

[36] R. Lou, B.-B. Fu, Q. N. Xu, P.-J. Guo, L.-Y. Kong, L.-K. Zeng, J.-Z. Ma, P. Richard, C. Fang, Y.-B. Huang *et al.*, Evidence of topological insulator state in the semimetal LaBi, Phys. Rev. B **95**, 115140 (2017).

[37] X. H. Niu, D. F. Xu, Y. H. Bai, Q. Song, X. P. Shen, B. P. Xie, Z. Sun, Y. B. Huang, D. C. Peets, and D. L. Feng, Presence of exotic electronic surface states in LaBi and LaSb, Phys. Rev. B **94**, 165163 (2016).

[38] S.-Y. Yang, Y. Wang, B. R. Ortiz, D. Liu, J. Gayles, E. Derunova, R. Gonzalez-Hernandez, L. Šmejkal, Y. Chen, S. S. P. Parkin *et al.*, Giant, unconventional anomalous Hall effect in the metallic frustrated magnet candidate, $KV_3Sb_5$, Sci. Adv. **6**, eabb6003 (2020).

[39] A. Mishra and S. Lee, Magnetic Chern insulators in a monolayer of transition metal trichalcogenides, Sci. Rep. **8**, 799 (2018); S. Baidya, A. V. Mallik, S. Bhattacharjee, and T. Saha-Dasgupta, Interplay of Magnetism and Topological Superconductivity in Bilayer Kagome Metals, Phys. Rev. Lett. **125**, 026401 (2020).

[40] R. Benedek and M. M. Thackeray, Simulation of the surface structure of lithium manganese oxide spinel, Phys. Rev. B **83**, 195439 (2011).

[41] D. Sen, G. Jana, N. Kaushal, A. Mukherjee, and T. Saha-Dasgupta, Intrinsic ferromagnetism in atomically thin two-dimensional organic-inorganic van der Waals crystals, Phys. Rev. B **102**, 054411 (2020).

[42] W. Wang, S. Dai, X. Li, J. Yang, D. J. Srolovitz, and Q. Zheng, Measurement of the cleavage energy of graphite, Nat. Commun. **6**, 7853 (2015).

[43] Y. Jing, Y. Ma, Y. Li, and T. Heine, $GeP_3$: A small indirect band gap 2D crystal with High carrier mobility and strong interlayer quantum confinement, Nano Lett. **17**, 1833 (2017).

[44] J. H. Jung, C. H. Park, and J. Ihm, A rigorous method of calculating exfoliation energies from first principles, Nano Lett. **18**, 2759 (2018).

[45] Y. Jiao, L. Zhou, F. Ma, G. Gao, L. Kou, J. Bell, S. Sanvito, and A. Du, Predicting single-layer technetium dichalcogenides ($TcX_2$, X = S, Se) with promising applications in photovoltaics

and photocatalysis, ACS Appl. Mater. Interfaces **8**, 5385 (2016).

[46] H. Wang, E. Liu, Y. Wang, B. Wan, C. H. Ho, F. Miao, and X. G. Wan, Cleavage tendency of anisotropic two dimensional materials: Re$X_2$ ($X$ = S, Se) and $WTe_2$, Phys. Rev. B **96**, 165418 (2017).

[47] M. A. McGuire, G. Clark, Santosh KC, W. M. Chance, G. E. Jellison, Jr., V. R. Cooper, X. Xu, and B. C. Sales, Magnetic behavior and spin-lattice coupling in cleavable van der Waals layered $CrCl_3$ crystals, Phys. Rev. Mater. **1**, 014001 (2017).

[48] S. Chabungbam and P. Sen, Computational design of a robust two-dimensional antiferromagnetic semiconductor, Phys. Rev. B **96**, 045404 (2017).

[49] K. Mondal and P. Ghosh, Exfoliation of $Ti_2C$ and $Ti_3C_2$ Mxenes from bulk trigonal phases of titanium carbide: A theoretical prediction, Solid State Commun. **299**, 113657 (2019).

[50] M. Naguib, V. N. Mochalin, M. W. Barsoum, and Y. Gogotsi, 25th anniversary article: MXenes: A new family of two-dimensional materials, Adv. Mater. **26**, 992 (2013).